Received: 17 May 2020 | Revised: 23 September 2020 | Accepted: 24 November 2020

DOI: 10.1002/aic.17147

TRANSPORT PHENOMENA AND FLUID MECHANICS

AIChE JOURNAL

Nanoparticle dispersion in porous media: Effects of hydrodynamic interactions and dimensionality

Deepak Mangal | **Jacinta C. Conrad** | **Jeremy C. Palmer**

Department of Chemical and Biomolecular Engineering, University of Houston, Houston, Texas

Correspondence
Jacinta C. Conrad and Jeremy C. Palmer, Department of Chemical and Biomolecular Engineering, University of Houston, Houston, Texas 77204, USA.
Email: jcconrad@uh.edu (J. C. C.) and
Email: jcpalmer@uh.edu (J. C. P.)

Funding information
Division of Chemical, Bioengineering, Environmental, and Transport Systems, Grant/Award Numbers: CBET-1751173, CBET-1803728; Welch Foundation, Grant/Award Numbers: E-1869, E-1882

Abstract

We investigate the effect of steric and hydrodynamic interactions (HI) on quiescent diffusion and flow-driven transport of finite-sized nanoparticles through periodic 2D (two-dimensional) and 3D (three-dimensional) nanopost arrays using Stokesian dynamics simulations. We find that steric and HI hinder particle diffusivity under quiescent conditions and enhance longitudinal dispersion under flow. Moreover, the presence of HI leads to a power-law increase in the longitudinal dispersion coefficient with Pe due to spatial variations in the fluid velocity. Lastly, our simulations reveal that longitudinal particle dispersion coefficients behave similarly in 2D and 3D when HI are included.

KEYWORDS
particle dispersion, confined transport, diffusion, Stokesian dynamics

1 | INTRODUCTION

Understanding the transport of nanoparticles through geometrically complex porous media is a problem with widespread implications in chemical engineering. Nanoparticles synthesized in solution, for example, are separated and purified using gel electrophoresis,[1] size-exclusion chromatography,[2] or membrane[3] processes, requiring particles to be transported through small channels or pores in gels, columns, or membranes. Nanoparticles used to enhance oil recovery,[4] by modifying the viscosity of sweep fluids[5] or the wetting properties of nearby interfaces,[6,7] must be transported to regions of low permeability within reservoirs. Similarly, the effectiveness of therapeutic nanoparticles depends on their ability to transport through narrow blood capillaries[8] or penetrate deep into tumors.[9,10] Finally, controlling the spatial distribution of nanoparticles flowed into confined geometries,[11] arising as one example during infiltration into a fiber matrix,[12] is required to attain the exceptional functional or mechanical properties of particle-laden nanocomposites.[13] In each of these applications, the particle size is comparable to the confining length scale, such as a pore or throat diameter. Hence, designing processes to deliver particles deep within a porous medium requires methods to understand the influence of physical interactions arising from strong confinement on particle transport.

Particle transport in a disordered medium has been traditionally described through macroscopic parameters such as tortuosity, porosity, and pore connectivity.[14,15] Both molecular diffusive and advective processes contribute to asymptotic (long-time) dispersion, and the relative contribution from each process is determined by the Péclet (Pe) number, the ratio of the rates of advective and diffusive transport. When particles are small compared to characteristic length scales within the medium, asymptotic dispersion is controlled by molecular diffusion when Pe is small and by advection when Pe is large.[16] Particle velocity profiles at the pore scale reflect the local spatial heterogeneity,[17] but do not affect asymptotic dispersion when Pe is large.[18] The use of macroscopic geometric parameters relies on the assumption that the disordered structure of the medium uniformly mixes the fluid,[14] such that the particles fully sample the void space within the medium.[19] If, instead, particles cannot fully sample the void space, deviations from this picture can arise. Particles flowed through ordered media, for example, may follow deterministic[20,21] or time-periodic[22,23] trajectories, so that transport is intimately coupled to geometry. Likewise, particles whose size is close to that of channels or voids in the medium may be excluded from accessing slow streamlines near surfaces.[24] As one consequence, particles move through the medium more rapidly and exhibit "early breakthrough" relative to tracers.[25,26] These examples suggest that, in many scenarios,

developing insight into the controlling physics[27] requires methods to link pore–scale interactions to macroscopic transport.

Particles whose size is comparable to length scales within the porous medium interact sterically and hydrodynamically with the medium during transport. Steric interactions make a fraction of the fluid volume in the porous medium inaccessible to the center of the particles, and hydrodynamic interactions (HI) lead to an increase in the drag force on the particles.[28,29] The importance of these physical interactions on particle dynamics has been investigated in several contexts. For example, steric and hydrodynamic interactions reduce particle diffusivity significantly in fibrous media.[30,31] Accurate modeling of HI is necessary to predict evolution of particle deposition in channel flow.[32] Finally, HI strongly affect the reorientation of particles at 2D interfaces and hence their aggregation kinetics.[33] There remains a need, however, to understand how steric and hydrodynamic interactions induced by nearby surfaces affect dispersion in strongly confined porous media.

Theoretical and computational studies of pore–scale transport have often focused on the dispersion of infinitesimally small particles. Approaches include the method of spatial moments, in spatially periodic porous media;[34] volume averaging, in both ordered and random porous media;[35] and particle tracking combined with the lattice Boltzmann method.[36] Because particles in these studies are very small, however, physical interactions with the medium do not play an important role in the dispersion. Probing the effects of physical interactions on the transport of finite-sized particles in porous media instead requires methods that can capture long-range HI. Stokesian dynamics (SD)[37] is a powerful method that can accurately account for HI between a particle and the porous medium. In this method, long-range, many-body HI are included via the far-field mobility matrix, and short-range lubrication interactions are included via a two-body resistance matrix.[37] This method has been successfully used to assess the applicability of the Brinkman equation to porous media,[38] to probe the dynamics of a suspension of rigid spherical particles in a Newtonian fluid,[39] and to investigate particle deposition, bridging, and cake formation during filtration.[40] It has been used to calculate local transport coefficients in studies of dispersion of a finite-sized particle in an array of parallel fibers for Péclet numbers $0 < Pe < 1$ using generalized Taylor dispersion theory.[41,42] Nonetheless, a complete understanding of the distinctive effects of steric and both near-field lubrication and far-field hydrodynamic interactions on particle dispersion in porous media remains elusive. Furthermore, open questions also remain about the effect of system dimensionality on transport and how dispersion processes differ in quasi-2D[43-45] and 3D systems.

In this paper, we investigate the effect of steric and hydrodynamic interactions on particle diffusion and dispersion in 2D (two-dimensional) and 3D (three-dimensional) periodic nanopost arrays, which are systems commonly used in fundamental studies of confined transport processes[43-45] and applications such as deterministic lateral displacement[20,46] and hydrodynamic chromatography .[47-49] We find that quiescent diffusion decreases with confinement, as expected, and this decrease is significantly enhanced by inclusion of HI. Under flow conditions, HI leads to markedly enhanced longitudinal dispersion at high Pe for all confinements. These behaviors are shown to arise from long-range HI between the particles and nanoposts as opposed to short-range lubrication forces. Lastly, when HI are included, we observe that system dimensionality has no qualitative effect on particle transport behavior, although some quantitative discrepancies are observed due to differences in modeling the porous media in 2D and 3D. Our study provides the necessary foundation for understanding the effects of HI and geometry on dispersion in realistic models of porous media.

2 | METHODS

To analyze the effect of system dimensionality on particle transport, we performed SD simulations of both 3D and 2D arrays of nanoposts. The 3D nanoposts were modeled as immobile chains of tangential spheres of diameter d_{np}. The chains were arranged on a square periodic lattice in the *xy*-plane, with their major axes aligned along the *z*-direction of the simulation cell (Figure 1a). This representation of the solid phase is similar to the well-established cylindrical fiber models that have been employed in previous SD simulations of confined particle transport.[41,42] Similar models have also been recently employed to investigate particle diffusion in hydrogel networks using SD.[30,31,50] The 2D nanoposts were modeled as the limiting case of the 3D systems in which the chains consist of only a single sphere in the *xy*-plane of the simulation cell (Figure 1b). In both the 3D and 2D systems, the nanopost arrays were oriented at 45° with respect to the incident flow direction (Figure 1b). The confinement length for the nanopost systems is the edge-to-edge spacing S between nanoposts (Figure 1b). This quantity, along with the diameter of the transported particle d_p, defines the dimensionless confinement parameter $\zeta = d_p/S$.

The simulations were performed under dilute conditions by considering the transport of only a single particle i with diameter d_p and mass m_i through the nanopost arrays. The motion of the particle is governed by the Langevin equation:

$$m_i \frac{d\mathbf{V}_i}{dt} = \mathbf{F}_i^{H}(t) + \mathbf{F}_i^{B}(t) + \mathbf{F}_i^{C}(t), \tag{1}$$

where $\mathbf{V}_i$ is the particle's velocity, and $\mathbf{F}_i^{H}$, $\mathbf{F}_i^{B}$, and $\mathbf{F}_i^{C}$ are the hydrodynamic, Brownian, and conservative forces acting on the particle, respectively.

In the low Reynolds number limit, the hydrodynamic forces acting on the particle are given by:

$$\mathbf{F}_i^{H}(t) = -\sum_{j=1}^{N_{np}+1} \mathbf{R}_{ij}^{FU} \cdot \left(\mathbf{V}_j - \mathbf{V}_\infty(\mathbf{r}_j)\right), \tag{2}$$

where N_{np} is the number of spheres composing the nanoposts in the simulation cell, $\mathbf{V}_j$ is the velocity of the jth sphere ($\mathbf{V}_j = 0 \;\forall\; j \in N_{np}$ for the immobile nanoposts considered here), and $\mathbf{V}_\infty(\mathbf{r}_j)$ is the

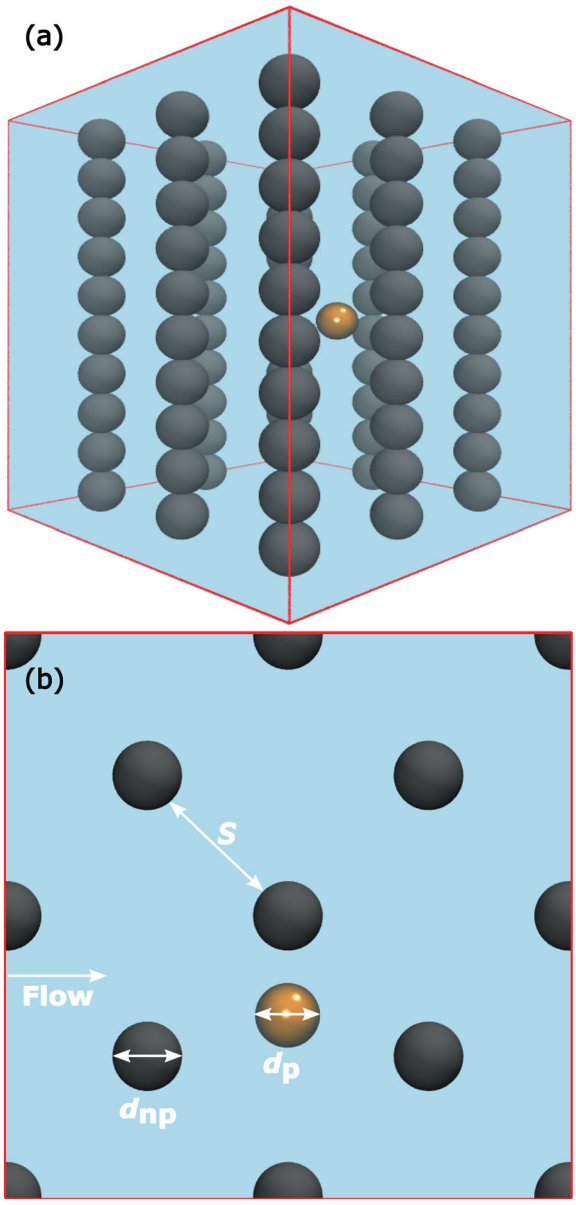

FIGURE 1 Model for the porous medium in (a) 3D and (b) 2D. The spheres representing the nanoposts (np) and the diffusing particle (p) have the same diameter (i.e., $d_{np} = d_p$) [Color figure can be viewed at wileyonlinelibrary.com]

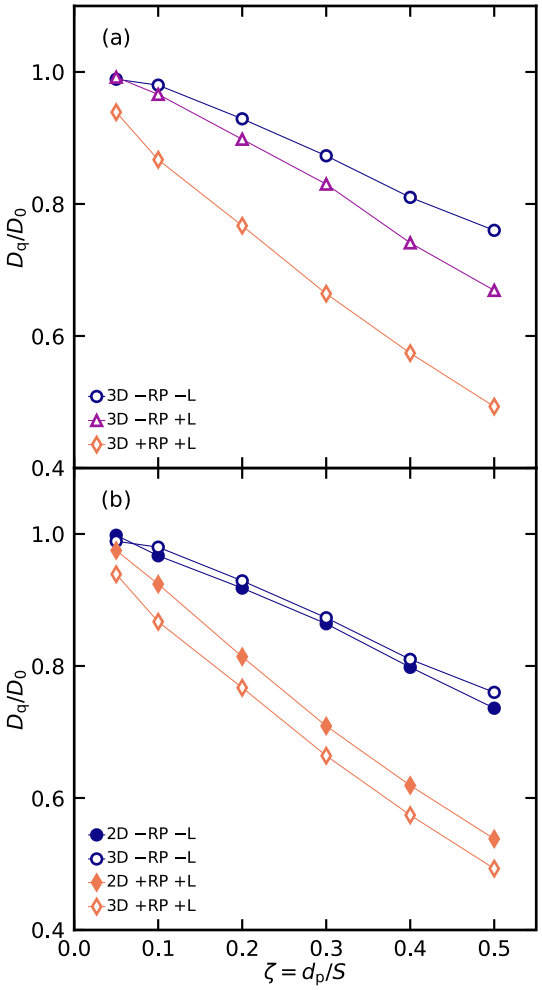

FIGURE 2 (a) Normalized particle diffusivity D_q/D_0 as function of dimensionless confinement parameter $\zeta = d_p/S$ for 3D systems from simulations with no HI (−RP − L, circles), lubrication interactions (−RP + L, triangles), and full HI (+RP + L, diamonds). (b) Comparison of normalized particle diffusivity between 2D and 3D systems (closed and open symbols, respectively) from simulations without HI (−RP − L, circles) and with full HI (+RP + L, diamonds). Estimated uncertainties are smaller than the symbols [Color figure can be viewed at wileyonlinelibrary.com]

unperturbed velocity of fluid evaluated at the sphere's center position $\mathbf{r}_j$. Using the adopted notation, the self-term for the diffusing particle (i.e., $i = j$) corresponds to $j = N_{np} + 1$ in Equation (2). In SD, the configuration-dependent resistance matrix $\mathbf{R}^{FU}$ is written as the sum of a far-field term $(\mathbf{M}^{\infty})^{-1}$ and a near-field lubrication correction $\mathbf{R}^{lub}$:

$$\mathbf{R}^{FU} = (\mathbf{M}^{\infty})^{-1} + \mathbf{R}^{lub}. \quad (3)$$

The far-field mobility matrix ($\mathbf{M}^{\infty}$) is evaluated via an Ewald sum of the Rotne–Prager (RP) tensor, using appropriate expressions derived for 3D (Reference 51; Appendix A) and 2D (Reference 52; Appendix A) systems. The matrix $\mathbf{R}^{lub}$ is calculated by subtracting the far-field two-particle RP contribution, which is already included in $(\mathbf{M}^{\infty})^{-1}$, from the full two-particle resistance tensor derived by Jeffrey and Onishi (Reference 53; Appendix B).

The stochastic Brownian force $\mathbf{F}_i^B$ on the particle arising from thermal fluctuations in the fluid is modeled as a Gaussian random variable satisfying $\left\langle \mathbf{F}_i^B \right\rangle = 0$ and the fluctuation–dissipation relation $\left\langle \mathbf{F}_i^B(t)\mathbf{F}_i^B(t+t') \right\rangle = 2k_B T \mathbf{R}_{ii}^{FU}\delta(t')$, where t and t' represent time, δ is the Dirac delta function, and $\mathbf{R}_{ii}^{FU}$ is the self-resistance matrix. In simulation, this force is calculated as $\mathbf{F}_i^B = \sqrt{2k_B T/dt}\mathbf{L}\cdot\boldsymbol{\xi}$, where k_B is Boltzmann's constant, T is temperature, and dt is the integration time step.[31] Each component of the vector $\boldsymbol{\xi}$ is a Gaussian random number with zero mean and unit variance, and $\mathbf{L}$ is a lower triangular matrix resulting from the Cholesky decomposition $\mathbf{R}_{ii}^{FU} = \mathbf{L}\cdot\mathbf{L}^T$.[54] Lastly, the conservative force $\mathbf{F}_i^C$ arises from hard-sphere repulsions between the

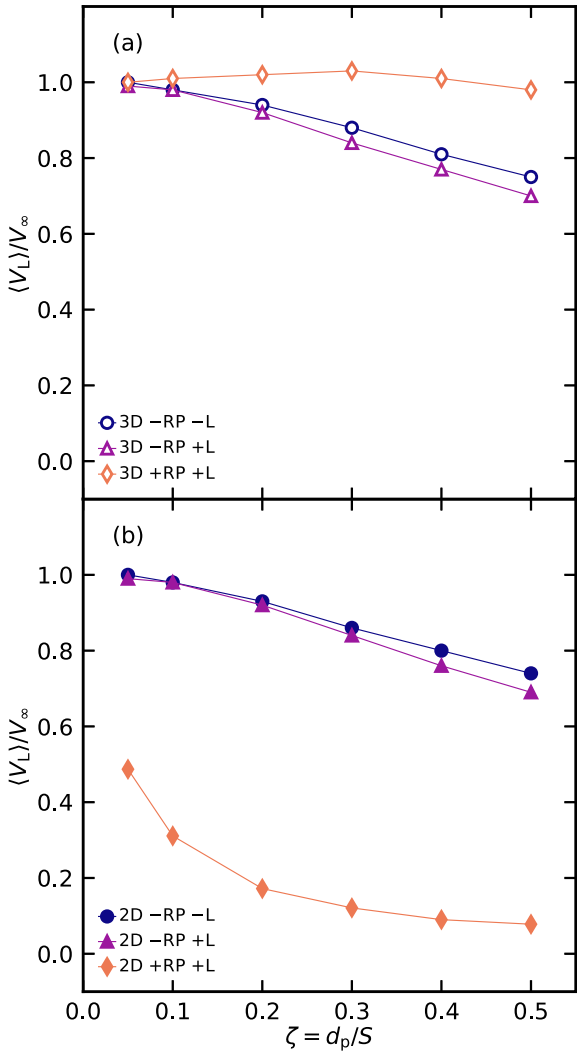

FIGURE 3 Normalized average particle velocity $\langle V_L \rangle / V_\infty$ as a function of dimensionless confinement parameter $\zeta = d_p/S$ for (a) 3D and (b) 2D systems (open and closed symbols, respectively) from simulations with no HI (−RP − L, circles), lubrication interactions (−RP + L, triangles), and full HI (+RP + L, diamonds). Estimated uncertainties are smaller than the symbols [Color figure can be viewed at wileyonlinelibrary.com]

particle and nanoposts, which were accounted for in our simulations using the standard rejection scheme.[30,31]

Integrating Equation (1) over a time dt that is large compared to the momentum relaxation time, but small compared to the diffusive time scale on which the particle position $\mathbf{r}_i$ changes significantly, yields the evolution equation[55]:.

$$\mathbf{r}_i(t+\mathrm{d}t) = \mathbf{r}_i(t) + \mathrm{d}t k_B T \nabla \cdot \left(\mathbf{R}_{ii}^{FU}\right)^{-1}(t) + \mathrm{d}t \left(\mathbf{R}_{ii}^{FU}\right)^{-1}(t) \cdot \left[\sum_{j=1}^{N_{np}+1} \mathbf{R}_{ij}^{FU}(t) \cdot \mathbf{V}_\infty(\mathbf{r}_j) + \mathbf{F}_i^B(t) + \mathbf{F}_i^C(t)\right]. \quad (4)$$

The particle position in the SD simulations was propagated via Equation (4), along with a modified mid-point scheme to evaluate the divergence of the self-mobility matrix $\nabla \cdot \left(\mathbf{R}_{ii}^{FU}\right)^{-1}(t)$ (Reference 56; Appendix C). An integration time step $dt = 5 \times 10^{-5} \tau_d$ was chosen to update the particle position, where $\tau_d = 3\pi\eta d_p^3/4k_BT$ is the diffusive time-scale and η is the dynamic fluid viscosity.

Stokesian dynamics is computationally intensive due to the calculation of the $3(N_{np}+1) \times 3(N_{np}+1)$ far-field resistance matrix $(\mathbf{M}^\infty)^{-1}$, which requires $\mathcal{O}\left(N^3\right)$ operations using standard matrix inversion algorithms.[54] Following Reference 31, we mitigate the cost of this inversion by taking advantage of the fact that $(\mathbf{M}^\infty)^{-1}$ only varies with the position of the mobile particle and hence can be pre-tabulated on a regularly spaced grid. Memory requirements associated with pre-tabulating this quantity were minimized by recognizing that the grid needs only to span a single unit cell of the nanopost arrays because of their periodicity. For our calculations, we used a grid spacing of 0.05 d_p; reducing the grid spacing further was found to have a negligible effect on the accuracy of the simulations. The matrix $\mathbf{R}^{lub}$, by contrast, was calculated on the fly due to its strong dependence on the separation distances between the particle and spheres in nearby nanoposts.

Modeling systems with long-range HI using periodic boundary conditions introduces well-known finite-size effects.[31,57-59] As a result, the dimensions of the simulation cell were carefully chosen to minimize these finite-size effects on computed properties. For the 3D system, we used a 3×3 array of nanoposts, modeling each post as a chain of 20 tangential spheres extending along the z-direction of the simulation cell. The diameter of each nanopost sphere was set equal to the particle diameter (i.e., $d_{np} = d_p$). For the 2D system, we used a 15×15 periodic array due to reduced screening of HI in 2D systems. In initial tests, the calculated particle diffusivities were found to be in statistical agreement with those obtained from simulations of significantly larger systems, indicating that the chosen dimensions were sufficient to minimize finite-size effects on particle transport properties. In performing the simulations, we adopted a set of reduced units in which d_p, k_BT, and τ_d were used as the fundamental measures of length, energy, and time, respectively, setting all equal to unity. We note that a fundamental measure of mass does not need to be specified to non-dimensionalize the particle's equations of motion (Equation (4)), as the SD algorithm is formulated in the low Re limit and thus neglects inertial effects. Comparison between the 3D and 2D systems was facilitated by computing all transport properties from the in-plane (x and y) coordinates of the particles. Transport properties were computed by averaging over 100 independent particle trajectories of length 1×10^9 time-steps, and statistical uncertainties were estimated from the standard error of the mean computed from the trajectories.

3 | RESULTS AND DISCUSSION

3.1 | Quiescent diffusion

Stokesian dynamics simulations were performed to examine the effect of steric and hydrodynamic interactions on quiescent diffusion in

confinement. We determined the particle diffusivity from the long-time limit of the ensemble-averaged, in-plane mean-square displacement, $D_q = \lim_{\Delta t \to \infty} \langle \Delta r^2(\Delta t) \rangle / 4\Delta t$, and compare across different confinements by normalizing by the diffusion coefficient of a freely diffusing particle $D_0 = k_B T / 3\pi\eta d_p$. To examine the effects of steric exclusion on particle diffusion, we carried out simulations in the 3D system without far-field hydrodynamic (−RP) or lubrication (−L) interactions. The normalized diffusivity D_q/D_0 is close to 1 for small values of the confinement parameter $\zeta = d_p/S$ and decreases monotonically with increasing ζ (Figure 2a), reflecting slowing of the particle's motion due to the higher frequency of collisions with nanoposts in highly confined systems.

Inclusion of lubrication interactions (−RP + L) does not strongly affect the particle diffusivity in 3D for small values of $\zeta \leq 0.1$ (Figure 2a). In more highly confined systems ($\zeta \geq 0.1$), however, these interactions result in smaller values of D_q/D_0 compared to the case where only steric interactions are present. The increasing reduction in diffusivity can be explained by the short-range nature of the lubrication interactions, which slow the motions of particles that approach within a surface-to-surface distance of $\sim d_p$ of the nanoposts. Hence, the effect of lubrication interactions on D_q/D_0 is most significant in highly confined systems (large ζ) due to the increased frequency of encounters with the nanoposts. These observations are consistent with those reported in earlier simulation studies of finite-sized particle diffusion in hydrogels,[30,31] which found that neglecting the lubrication correction led to a slightly higher diffusivity compared to that calculated with full HI (+RP + L). The addition of far-field interactions (+RP + L) reduces the particle diffusivity by 4% for small $\zeta = 0.05$ and by 18% for large $\zeta = 0.5$ compared to corresponding values of D_q/D_0 with lubrication interactions (−RP + L) (Figure 2a). For $\zeta \geq 0.3$, the effect of far-field HI becomes almost constant, whereas lubrication interactions play an increasing role as confinement is strengthened. Overall, the trend of decreasing diffusivity with increasing confinement is consistent with an earlier experimental study that shows a linear relationship between relative diffusivity and confinement over a similar confinement range.[43]

Finally, we explored the effect of dimensionality by comparing diffusivities obtained from simulations in 2D and 3D, with and without HI (Figure 2b). In the absence of HI (−RP − L), the normalized particle diffusivities in the 3D and 2D systems are nearly identical, exhibiting maximum deviation of 2% at the strongest confinement ($\zeta = 0.5$) examined. This agreement is due to the similarity of the steric excluded volume interactions between particles and nanoposts in the 3D and 2D systems. When HI are turned on (+RP + L), however, the values of D_q/D_0 in 3D are approximately 4% lower than those for the corresponding 2D systems. This reduction arises from the representation of the nanoposts as chains of spheres in 3D, which results in increased hydrodynamic drag compared to the single sphere nanopost model used in the 2D systems. This result is in agreement with previous experimental and theoretical studies which have shown that the sphere–cylinder resistance coefficient is larger than the sphere–sphere resistance coefficient.[60,61]

3.2 | Average velocity and trajectory metrics

Stokesian dynamics simulations were also performed to investigate the effect of steric and hydrodynamic interactions on flow-driven particle transport in confinement. A uniform suspension velocity with magnitude $|\mathbf{V}_\infty(\mathbf{r})| = V_\infty$ was imposed in the simulations to mimic pressure-driven flow through the nanopost arrays (Equation (2); References 41 and 42). We first examine the normalized average longitudinal particle velocity (velocity in the direction of flow) $\langle V_L \rangle / V_\infty$ estimated from linear fits to the ensemble-average of the particle displacements over time. In the absence of HI (−RP − L), the average particle velocity in the 3D systems monotonically decreases with increasing ζ (Figure 3a). Including near-field lubrication interactions (−RP + L) only slightly reduces the average particle velocity even for strong confinement. The addition of far-field HI (+RP + L), however, dramatically changes the scaling behavior, causing $\langle V_L \rangle / V_\infty$ to vary weakly ($\lesssim$10%) with ζ over the range of confinements investigated and exhibit a local maximum at $\zeta \approx 0.3$. Similar trends in the average particle velocity with increasing confinement for 3D systems with full HI (+RP + L), including the weakly non-monotonic behavior, were theoretically predicted for particles flowing in cylindrical pores[28] and in periodic porous media.[41,42] The striking contrast between scaling of velocities in simulations with and without far-field HI indicates that far-field HI strongly affect the transport of particles in porous media.

Differences in the dependence of the average velocity on confinement in the presence and absence of HI have various physical origins. When far-field HI and lubrication interactions are excluded (−RP − L), Equation (2) reduces to $\mathbf{F}_i^H = 3\pi\eta d_p(\mathbf{V}_i(t) - \mathbf{V}_\infty)$, yielding a spatially uniform viscous drag on the particle. Thus, in this case, the decrease in the average particle velocity observed in both the 3D and 2D systems reflects increasing steric hindrance from the nanoposts as ζ is increased. A similar decrease in velocity with increasing confinement has also been reported in Brownian dynamics simulations without HI (−RP − L) of force-driven particle transport through ordered porous media.[62,63] Inclusion of near-field lubrication interactions (−RP + L) slows particle motion near the nanopost in both 3D and 2D, further reducing the average particle velocity in strongly confined systems. Interestingly, in contrast to the other two cases, inclusion of far-field hydrodynamics (+RP + L) leads to qualitative differences in the average particle velocity in the 3D and 2D systems (Figure 3b). This discrepancy arises from the different representations of nanoposts in 3D and 2D. To illustrate this fact, we analyze the velocity of a particle in the absence of Brownian fluctuations, $\mathcal{V}$. In the small Reynolds number limit, the particle's equation of motion (Equation (1)) simplifies to $\mathbf{F}_i^H = 0$. Imposing this condition on Equation (2) and rearranging yields an expression for the particle's local velocity:

$$\mathcal{V}(\mathbf{r}_i) = \mathbf{V}_\infty(\mathbf{r}_i) + \left(\mathbf{R}_{ii}^{FU}\right)^{-1} \left(\sum_{j=1 \neq i}^{N_{np}+1} \mathbf{R}_{ij}^{FU} \cdot \mathbf{V}_\infty(\mathbf{r}_j) \right). \quad (5)$$

Equation (5) can be spatially averaged over the sterically accessible (fluid) regions of the nanopost systems to obtain the particle's

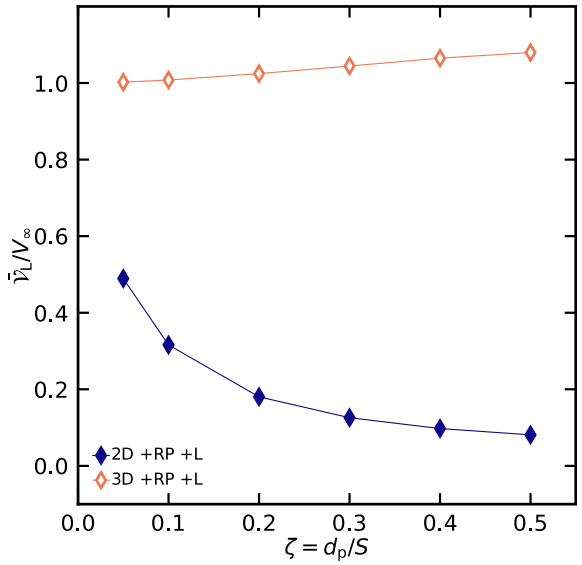

FIGURE 4 Normalized spatial average velocity $\bar{\mathcal{V}}_L/V_\infty$ induced by nanoposts in the 2D and 3D systems (closed and open symbols, respectively) [Color figure can be viewed at wileyonlinelibrary.com]

average velocity $\bar{\mathcal{V}}$. This time-independent quantity depends only on the geometry of the system and provides insights into how HI with the nanoposts influence the particle's mobility in the direction of flow. The longitudinal component of the spatial-average velocity $\bar{\mathcal{V}}_L$ increases slightly with ζ in 3D, whereas it decreases sharply with ζ in 2D (Figure 4). These trends follow those observed for $\langle V_L \rangle$ (Figure 3a, b), confirming that HI arising from particle-nanopost interactions dominate the behavior of the longitudinal velocity.

The morphology of the particle trajectories under flow was also characterized using metrics that describe the loss of directional persistence. First, we calculated the asymptotic tortuosity

$$\langle \tau \rangle = \lim_{n\to\infty} \langle \tau_n \rangle = \lim_{n\to\infty} \left\langle \sum_{i=1}^{n} L_i/\Delta L_n \right\rangle, \tag{6}$$

where L_i is the distance between two points along a particle trajectory separated by time-interval δt, ΔL_n is the end-to-end distance between points separated by time-interval $n\delta t$, and $\langle ... \rangle$ denotes the average over the ensemble of particle trajectories under the same flow and confinement conditions. Similarly, we also calculated the asymptotic cosine of the correlation angle

$$\langle \cos\chi \rangle = \lim_{n\to\infty} \langle \cos\chi_n \rangle = \lim_{n\to\infty} \left\langle \hat{\mathbf{V}}(t) \cdot \hat{\mathbf{V}}(t+n\delta t) \right\rangle, \tag{7}$$

where $\hat{\mathbf{V}}(t)$ and $\hat{\mathbf{V}}(t+n\delta t)$ are the instantaneous unit particle velocity vectors at time t and $t+n\delta t$, respectively. The instantaneous velocity $\mathbf{V}(t)$ is calculated from two consecutive points separated by a time interval δt:

$$\mathbf{V}(t) = (\mathbf{r}_i(t+\delta t) - \mathbf{r}_i(t))/\delta t. \tag{8}$$

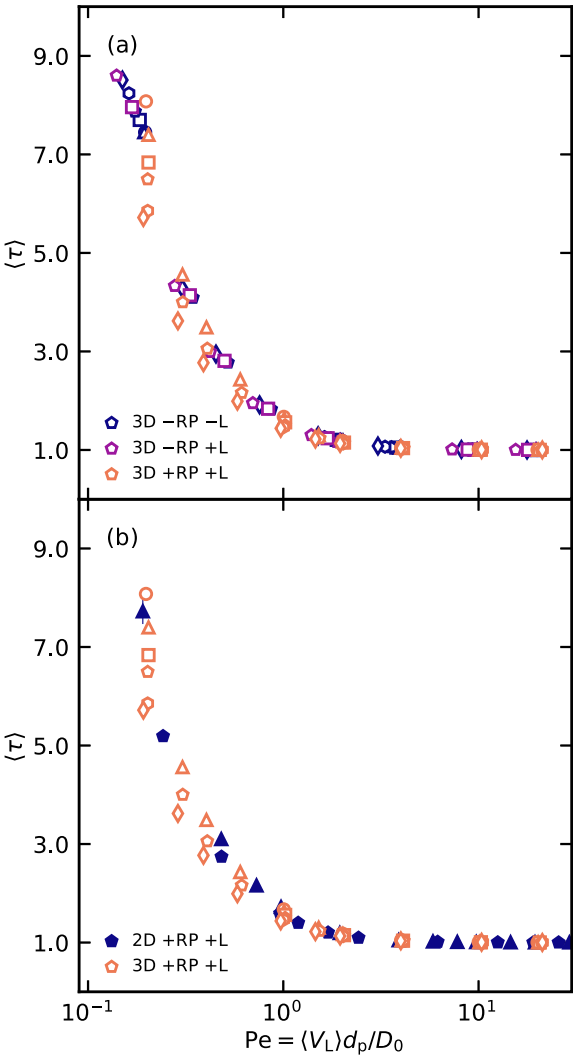

FIGURE 5 (a) Average tortuosity $\langle \tau \rangle$ as a function of Péclet number Pe for 3D systems. The different symbol shapes correspond to different confinements. (b) Comparison between 2D and 3D systems (closed and open symbols, respectively) from simulations with full HI (+RP + L). Estimated uncertainties are smaller than the symbols [Color figure can be viewed at wileyonlinelibrary.com]

In practice, $\langle \tau \rangle$ and $\langle \cos\chi \rangle$ were estimated from the values of $\langle \tau_n \rangle$ and $\langle \cos\chi_n \rangle$, respectively in the region where these functions plateau at large, but finite n.

Both metrics were calculated using $\delta t = 6\tau_d$ and analyzed as functions of the Péclet number $\mathrm{Pe} = \langle V_L \rangle d_p/D_0$. Independent of the nature of the HI included in the simulations of the 3D nanopost systems, the asymptotic tortuosity $\langle \tau \rangle$ sharply decreases and approaches one as Pe is increased (Figure 5a), indicating that the trajectories of the particles transported through the model porous media become increasingly linear. Likewise, the asymptotic $\langle \cos\chi \rangle$ increases from zero at low Pe to one at high Pe (Figure 6a). This behavior is consistent with a transition from diffusion-dominated transport at low Pe, for which the directions of the instantaneous velocities are expected to be essentially uncorrelated, to advection-dominated transport at high Pe, for which

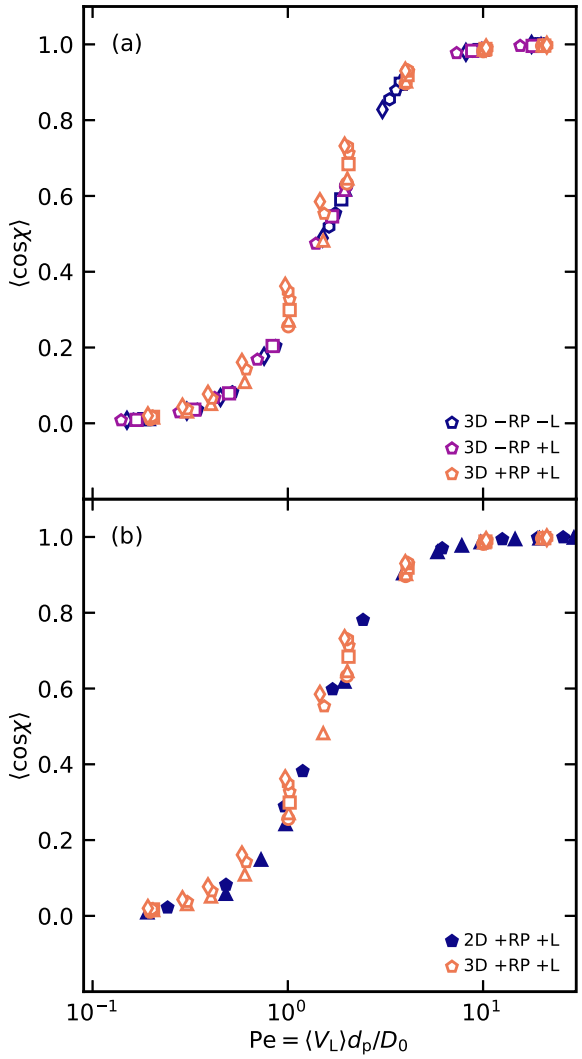

FIGURE 6 (a) Average cosine of angle between velocity vectors $\langle \cos\chi \rangle$ as a function of Péclet number Pe for 3D systems. The different symbol shapes correspond to different confinements. (b) Comparison between 2D and 3D systems (closed and open symbols, respectively) from simulations with full HI (+RP + L). Estimated uncertainties are smaller than the symbols [Color figure can be viewed at wileyonlinelibrary.com]

the velocity vectors are expected to be strongly directionally correlated. These observations are qualitatively consistent with those reported in an experimental study of nanoparticle transport in periodic post arrays for $0 < Pe < 100$.[44] The fact that $\langle \tau \rangle$ and $\langle \cos\chi \rangle$ obtained from simulations in both 3D and 2D (Figures 5b and 6b), with and without HI, each collapse on a single curve suggests that these metrics are independent of system dimensionality and a function only of the average particle velocity.

3.3 | Dispersion coefficients

To quantify the extent of spreading of particles through the nanopost systems under flow conditions, we calculated the asymptotic dispersion coefficients $D_{L,T}$ in the longitudinal (L) and transverse (T) directions. These phenomenological coefficients appear in the macroscale convection–diffusion equation, and are used in characterizing and modeling particle transport through porous media in applications including size-exclusion chromatography[2] and deep-bed filtration.[40] Previous studies have examined the effects of flow conditions[64-67] and characteristics of the confining medium, including long-range structural order,[64,66] local packing geometry,[64,65] and pore shape,[67] on the transport of infinitesimal tracers. The effects of porosity,[41,42] particle size, and fiber configurations[42] on the transport of finite-sized particles in a spatially periodic fibrous medium have also been studied computationally. Nonetheless, the influence of HI on the dispersion of finite-size particles remains incompletely understood.

The coefficients $D_{L,T}$ can be calculated directly from particle velocity auto-correlation functions.[36] Alternatively, as done in our analysis, they can be estimated from the asymptotic behavior of the particle mean-square displacements (MSDs), evaluated in the frame of reference of the average velocity of the particle ensemble $\langle V_{L,T} \rangle$ via[36,68]:

$$D_{L,T} \equiv \lim_{t\to\infty} \frac{1}{2} \frac{d\sigma^2_{L,T}(t)}{dt}, \tag{9}$$

where $\sigma^2_{L,T}(t) = \left\langle \left(\Delta r_{L,T}(t) - \langle V_{L,T} \rangle t\right)^2 \right\rangle$. Under quiescent conditions, $\langle V_{L,T} \rangle = 0$ and Equation (9) reduces to the usual expression for the equilibrium diffusivity D_q. Hence, D_q provides a convenient normalization for the dispersion coefficients.

Under moderate confinement in 3D ($\zeta = 0.3$), D_L/D_q is approximately constant and relatively insensitive to the presence or absence of lubrication and far-field hydrodynamic interactions at low Pe (Figure 7a). At large Pe, however, the scaling behavior of D_L/D_q depends on the treatment of the HI. In the absence of lubrication and far-field HI (−RP − L), D_L/D_q increases slightly with Pe. Longitudinal dispersion is further increased at $Pe \gtrsim 10$ by the inclusion of lubrication forces (−RP + L). Addition of far-field HI (+RP + L) results in an even more dramatic increase in D_L/D_q at high Pe, causing D_L/D_q to vary by more than an order of magnitude over the range of flow conditions examined. These results show that both near- and far-field HI enhance longitudinal dispersion.

The scaling behavior of the normalized transverse dispersion coefficient D_T/D_q, by contrast, is less sensitive to the treatment of HI. At low Pe, D_T/D_q remains approximately constant (Figure 7b). When only steric (−RP − L) and lubrication (−RP + L) interactions are present, D_T/D_q decreases slightly with Pe for $Pe \gtrsim 10$. When far-field HI are included, however, D_T/D_q remains nearly constant across the entire range of Pe examined.

The sensitivity of the dispersion coefficients to the treatment of HI arises from changes in the velocity field due to these interactions. In the absence of lubrication forces and far-field HI (−RP − L), the velocity field is uniform and dispersion is affected by particle diffusion and steric collisions with the nanoposts. The steric collisions slow the motions of particles, leading to slower dynamics of particles that

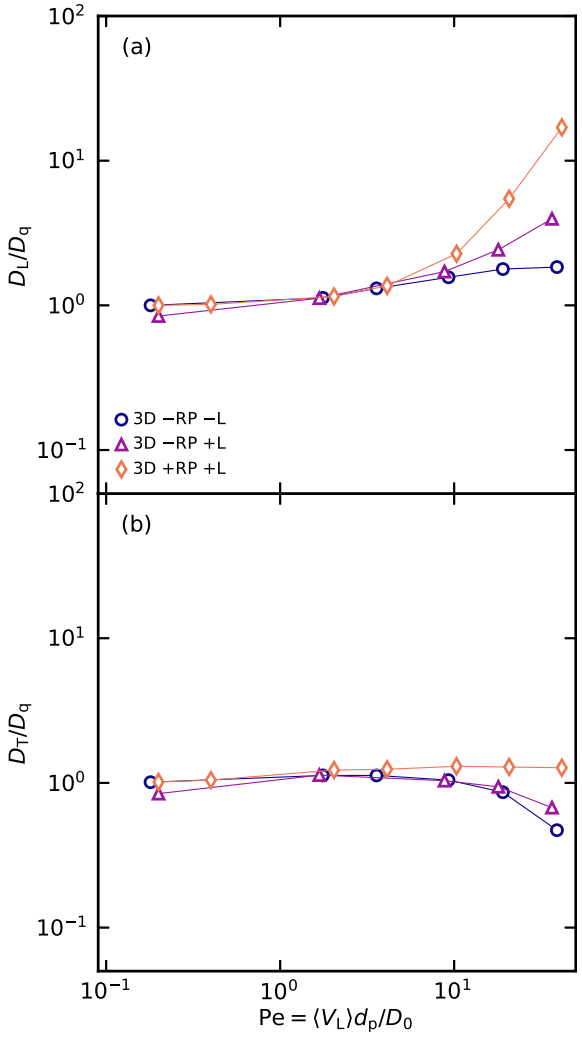

FIGURE 7 Normalized asymptotic (a) longitudinal (D_L/D_q) and (b) transverse (D_T/D_q) dispersion coefficients as a function of Péclet number Pe for confinement parameter ζ = 0.3 in 3D systems from simulations with no HI (−RP − L, circles), lubrication interactions (−RP + L, triangles), and full HI (+RP + L, diamonds). Estimated uncertainties are smaller than the symbols [Color figure can be viewed at wileyonlinelibrary.com]

collide more frequently with the nanoposts. As the flow rate is increased (Pe is increased), both the collision frequency and the width of the collision frequency distribution increase, leading to a broadening of the particle displacement distribution in the longitudinal direction and hence enhanced dispersion. This effect is only appreciable for $1 \lesssim Pe \lesssim 40$ where advection and diffusion contribute to transport and collisions lead to large changes in particle velocities along the direction of flow. At higher Pe ($\gtrsim$40), strong advection does not further increase collisions and the width of the collision frequency distribution narrows, leading to a weak local maximum in D_L/D_q. In the transverse direction, dispersion is dominated by diffusion for all Pe due to the absence of flow in that direction. The increase in particle–nanopost collisions at high flow rates ($Pe \gtrsim 10$) hinders particle diffusion, leading to a concomitant decrease in D_T/D_q at high Pe. Our results are consistent with an earlier study of Brownian transport of particles through an ordered cubic array of spheres under constant external force and in the absence of HI for 0 < Pe < 100.[62] In that study, the longitudinal dispersion coefficient exhibited a weak local maximum at intermediate Pe, whereas the transverse dispersion coefficient monotonically decreased with Pe.[62] The non-monotonic behavior of the longitudinal dispersion coefficient was associated with an external force threshold that was estimated by balancing the convection time with the time required for a particle to laterally diffuse around an obstacle.[62]

The addition of lubrication forces (−RP + L) increases the effective range of interactions with the nanoposts and introduces spatial variations in the velocity field, both of which enhance longitudinal dispersion. Inclusion of far-field HI (+RP + L) further increases spatial variations in the fluid velocity field, resulting in a more pronounced increase in D_L/D_q at high Pe. Spatial variations in fluid velocity in the transverse direction also appear upon inclusion of lubrication forces and far-field HI. Nonetheless, particle transport in the transverse direction remains diffusion-controlled because there is no net flow in that direction. Therefore, only a very modest increase is observed in the transverse dispersion coefficient with the inclusion of lubrication forces and far-field HI at high Pe. The power-law increase in D_L/D_q and weak increase in D_T/D_q with Pe (Figure 7) are consistent with several earlier studies examining the effects of near-field and far-field HI on dispersion of infinitesimal tracers. For example, theoretical analyses of tracer dispersion in the presence of HI through an ordered cubic array of spheres[66] and 2D periodic porous media[64,65] also predict a power-law dependence on Pe for the longitudinal dispersion coefficient at high Pe. These studies, which considered spatial variations in fluid velocity through the porous media, also found a weak dependence on Pe for the transverse dispersion coefficient across 0.1 < Pe < 1,000.

We also analyzed the effects of confinement and dimensionality by comparing dispersion coefficients for ζ = 0.05 and 0.30 in 2D and 3D systems. In the absence of lubrication and far-field HI (−RP − L), strong confinement results in an increase and decrease, respectively, in D_L/D_q and D_T/D_q at large Pe in 3D (Figure 8a,c). In the absence of these interactions, we do not observe any effect of dimensionality on either longitudinal or transverse dispersion coefficients. With inclusion of lubrication forces and far-field HI (+RP + L), however, strong confinement in 3D (ζ = 0.30) results in a decrease in D_L/D_q at high Pe, whereas D_T/D_q remains largely unchanged (Figure 8b,d). Moreover, with full HI (+RP + L) we observe that dimensionality does affect dispersion. The longitudinal dispersion coefficient in 3D is larger than that in the corresponding 2D case. Transverse dispersion is also larger in 3D than in the corresponding 2D for strong confinement ζ = 0.3, but dimensionality does not affect D_T/D_q for very weak confinement ζ = 0.05.

The variation in dispersion coefficients with confinement arises from the distinct effects of steric and hydrodynamic interactions. In the absence of lubrication and far-field HI (−RP − L), strong confinement leads to an increase in the frequency of collisions with nanoposts and the width of the collision frequency distribution,

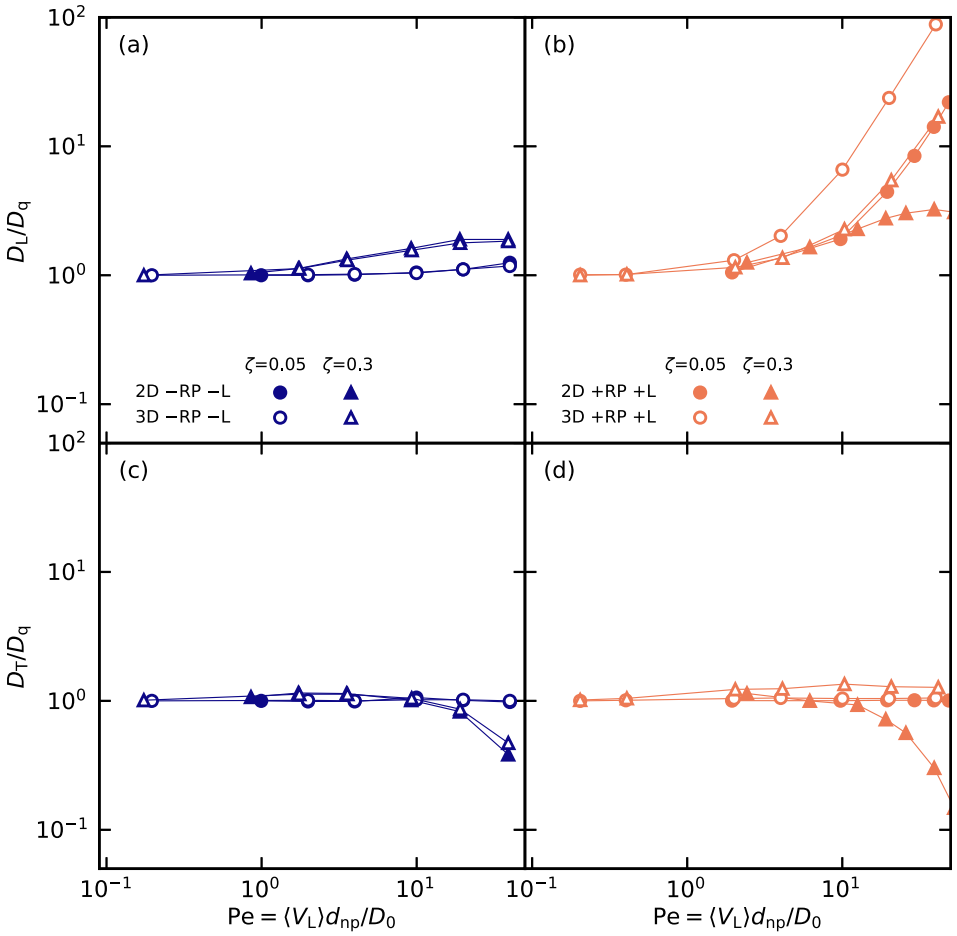

FIGURE 8 Comparison of normalized asymptotic dispersion coefficients for 2D and 3D systems (closed and open symbols, respectively). (a,b): Longitudinal dispersion coefficients from simulations (a) with no HI (−RP − L) and (b) with full HI (+RP + L). (c,d): Transverse dispersion coefficients from simulations (c) with no HI (−RP − L) and (d) with full HI (+RP + L). Circles and triangles represent confinements of $\zeta = 0.05$ and $\zeta = 0.3$, respectively. Estimated uncertainties are smaller than the symbols [Color figure can be viewed at wileyonlinelibrary.com]

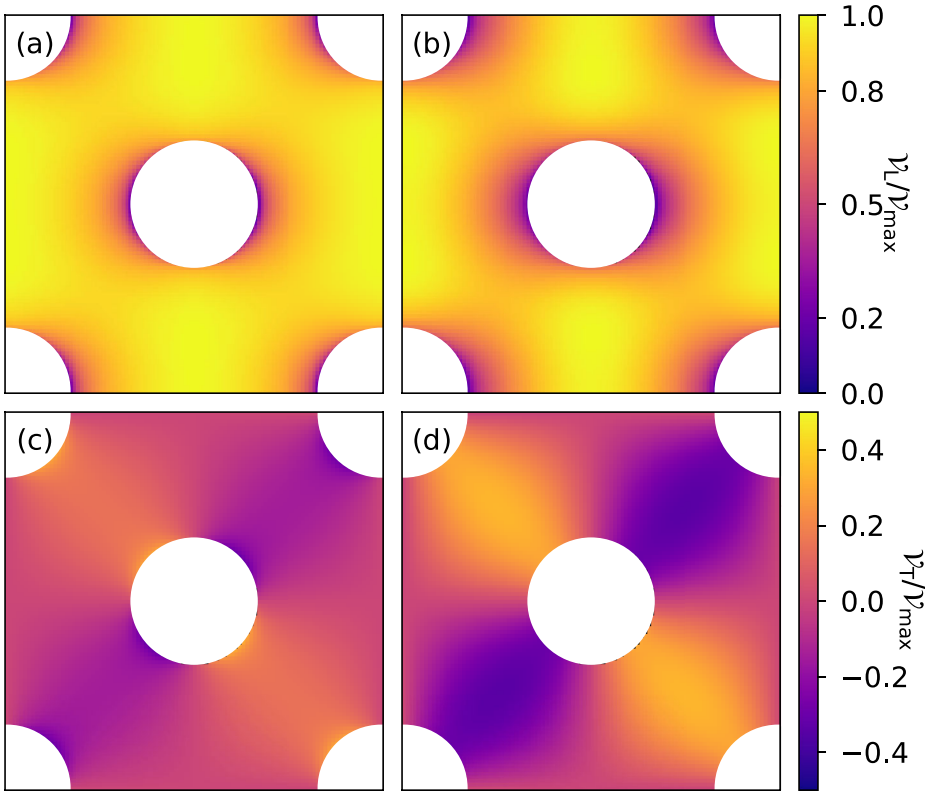

FIGURE 9 Local particle velocity field in the (a,b) longitudinal and (c,d) transverse directions normalized by the maximum longitudinal fluid velocity for (a,c) 2D and (b,d) 3D systems from simulations with $\zeta = 0.3$ and with full HI (+RP + L) [Color figure can be viewed at wileyonlinelibrary.com]

resulting in broadening of the particle displacement distribution in the longitudinal direction and hence an increase in D_L/D_q. Transverse dispersion, however, is dominated by diffusion due to the absence of flow in that direction. Strong confinement thus increases D_L/D_q but reduces D_T/D_q at high Pe. Our results are consistent with those reported in a previous simulation study of the transport of Brownian particles through an ordered cubic array of spheres under a constant external force and in the absence of HI.[62] That study also reported an increase and a decrease in D_L and D_T, respectively, at high Pe with increasing confinement.[62] With full HI (+RP + L), however, the presence of the nanoposts induces spatial variations in the fluid velocity that become more pronounced as confinement increases. These variations enhance longitudinal dispersion, but are counteracted by the narrowing in the distribution of streamlines sterically accessible to particles in strong confinement. Thus, in the presence of full HI (+RP + L), increased confinement results in an overall reduction of D_L/D_q at high Pe. The normalized transverse dispersion coefficient D_T/D_q from simulations with full HI (+RP + L), by contrast, remains approximately constant as confinement is increased because dispersion in that direction remains controlled by diffusion rather than advection. Further analysis of D_L/D_q as a function of ζ from the simulations with full HI (not shown) reveals qualitative agreement with Taylor–Aris dispersion theory, which predicts $D_L \propto a^2$ for Pe $\gg$ 1, where a is the diameter of a cylindrical pore.[69]

To understand the different scaling behaviors observed in 2D and 3D for simulations with full HI (+RP + L), we analyzed the local particle velocity field in longitudinal and transverse directions in the xy-plane and in the absence of Brownian force (Equation (5)). The local velocity field exhibits greater variations in the longitudinal direction in 3D than in 2D (Figure 9a,b) due the different representation of the nanoposts. The greater spatial variations in 3D result in enhanced dispersion (Figure 8b). Despite the stronger spatial variations in 3D (Figure 9c,d), tranverse transport remains diffusion controlled and thus D_T/D_q exhibits a weak dependence on Pe for both confinements. Due to the relatively weak spatial variations in the fluid velocity in 2D, however, steric interactions with the nanoposts dominate transverse dispersion, leading to a decrease in D_T/D_q with Pe in strong confinement (ζ = 0.3) and behavior that is independent of Pe for weak confinement (ζ = 0.05).

4 | CONCLUSIONS

We performed Stokesian dynamics simulations to examine the effect of steric and HI on quiescent diffusion and flow-driven transport of particles through 2D and 3D nanopost arrays. In the absence of lubrication forces and far-field HI (−RP − L), the quiescent particle diffusivity decays monotonically as the dimensionless confinement parameter ζ is increased because particles collide more frequently with the nanoposts. Hydrodynamic interactions (+RP + L) further reduce particle diffusivity by increasing the drag on the particle. Dimensionality does not affect diffusivity in the absence of lubrication and far-field HI. With full HI (+RP + L), however, particle diffusivity in 2D is slightly higher than that in the corresponding 3D system because the hydrodynamic drag from the nanoposts is lower in 2D. The longitudinal and transverse dispersion coefficient slightly increase and decrease, respectively, at large Pe in absence of lubrication forces and far-field HI (−RP − L). With inclusion of full HI (+RP + L), however, the presence of nanoposts generates spatial variations in the fluid velocity. As a result, the longitudinal dispersion coefficient increases as a power law at large Pe, whereas the transverse dispersion coefficient depends only weakly on Pe. These results suggest that steric and HI that hinder particle diffusivity under quiescent conditions enhance longitudinal dispersion under flow.

Our study provides insights into the effects of steric interactions and HI on finite-sized particles in ordered arrays, relevant to separations methods such as deterministic lateral displacement[20,46] and hydrodynamic chromatography.[47-49] For these systems, our simulations suggest that long-range HI are important even in weak confinement, but additional work is needed to ascertain whether these results are generalizable. For example, whereas we consider spherical particles here, significant work has been carried out examining (bio) polymer transport through similar ordered media.[70-72] Nonetheless, understanding the role of both short- and long-range HI on polymer transport through porous media remains an active area of research.[72-74] Additionally, extending the insights from our investigation to many scenarios of practical interest will require examining the role of spatial disorder in the porous medium and of non-steric (e.g., depletion or electrostatic) interactions between the particles and medium. We anticipate that computational approaches similar to those employed here can be used to address these questions in future studies.

ACKNOWLEDGMENTS

This work was supported by Welch Foundation (Grants E-1882 and E-1869 to JCP and JCC, respectively) and the National Science Foundation (CBET-1751173 (JCP) and CBET-1803728 (JCC)). Computational resources were generously provided by the Hewlett Packard Enterprise Data Science Institute at the University of Houston and the Texas Advanced Computing Center at the University of Texas at Austin.

AUTHOR CONTRIBUTIONS

Deepak Mangal: Conceptualization; data curation; formal analysis; investigation; methodology; software; writing-original draft; writing-review and editing. **Jacinta Conrad:** Conceptualization; funding acquisition; investigation; project administration; supervision; writing-original draft; writing-review and editing. **Jeremy Palmer:** Conceptualization; funding acquisition; investigation; methodology; project administration; supervision; writing-original draft; writing-review and editing.

ORCID

Jacinta C. Conrad https://orcid.org/0000-0001-6084-4772
Jeremy C. Palmer https://orcid.org/0000-0003-0856-4743

REFERENCES

1. Hanauer M, Pierrat S, Zins I, Lotz A, Sönnichsen C. Separation of nanoparticles by gel electrophoresis according to size and shape. *Nano Lett*. 2007;7(9):2881-2885.
2. Satzer P, Wellhoefer M, Jungbauer A. Continuous separation of protein loaded nanoparticles by simulated moving bed chromatography. *J Chromatogr A*. 2014;1349:44-49.
3. Krieg E, Weissman H, Shirman E, Shimoni E, Rybtchinski B. A recyclable supramolecular membrane for size-selective separation of nanoparticles. *Nat Nanotechnol*. 2011;6(3):141-146.
4. ShamsiJazeyi H, Miller CA, Wong MS, Tour JM, Verduzco R. Polymer-coated nanoparticles for enhanced oil recovery. *J Appl Polym Sci*. 2014;131(15):40576.
5. Dastvareh B, Azaiez J. Instabilities of nanofluid flow displacements in porous media. *Phys Fluids*. 2017;29(4):044101.
6. Zhang H, Nikolov A, Wasan D. Enhanced oil recovery (EOR) using nanoparticle dispersions: underlying mechanism and imbibition experiments. *Energy Fuel*. 2014;28(5):3002-3009.
7. Moghaddam RN, Bahramian A, Fakhroueian Z, Karimi A, Arya S. Comparative study of using nanoparticles for enhanced oil recovery: wettability alteration of carbonate rocks. *Energy Fuel*. 2015;29(4):2111-2119.
8. Fullstone G, Wood J, Holcombe M, Battaglia G. Modelling the transport of nanoparticles under blood flow using an agent-based approach. *Sci Rep*. 2015;5:10649.
9. Wong C, Stylianopoulos T, Cui J, et al. Multistage nanoparticle delivery system for deep penetration into tumor tissue. *Proc Natl Acad Sci*. 2011;108(6):2426-2431.
10. Vlashi E, Kelderhouse LE, Sturgis JE, Low PS. Effect of folate-targeted nanoparticle size on their rates of penetration into solid tumors. *ACS Nano*. 2013;7(10):8573-8582.
11. Chandran S, Begam N, Padmanabhan V, Basu JK. Confinement enhances dispersion in nanoparticle–polymer blend films. *Nat Commun*. 2014;5:3697.
12. Liu Y, Kumar S. Polymer/carbon nanotube nano composite fibers—a review. *ACS Appl Mater Interfaces*. 2014;6(9):6069-6087.
13. Kumar SK, Krishnamoorti R. Nanocomposites: structure, phase behavior, and properties. *Annu Rev Chem Biomol Eng*. 2010;1:37-58.
14. Saffman PG. A theory of dispersion in a porous medium. *J Fluid Mech*. 1959;6(03):321-349.
15. Whitaker S. Diffusion and dispersion in porous media. *AICHE J*. 1967;13(3):420-427.
16. Scheven UM. Pore-scale mixing and transverse dispersivity of randomly packed monodisperse spheres. *Phys Rev Lett*. 2013;110(21):214504.
17. Datta SS, Chiang H, Ramakrishnan TS, Weitz DA. Spatial fluctuations of fluid velocities in flow through a three-dimensional porous medium. *Phys Rev Lett*. 2013;111(6):064501.
18. Scheven UM, Harris R, Johns ML. Intrinsic dispersivity of randomly packed monodisperse spheres. *Phys Rev Lett*. 2007;99(5):054502.
19. Koch DL, Brady JF. Dispersion in fixed beds. *J Fluid Mech*. 1985;154:399-427.
20. Huang LR, Cox EC, Austin RH, Strum JC. Continuous particle separation through deterministic lateral displacement. *Science*. 2004;304(5673):987-990.
21. Frechette J, Drazer G. Directional locking and deterministic separation in periodic arrays. *J Fluid Mech*. 2009;627:379-401.
22. Hlushkou D, Piatrusha S, Tallarek U. Impact of diffusion on transverse dispersion in two-dimensional ordered and random porous media. *Phys Rev E*. 2017;95(6):063108.
23. Jacob JDC, Krishnamoorti R, Conrad JC. Particle dispersion in porous media: differentiating effects of geometry and fluid rheology. *Phys Rev E*. 2017;96(2):022610.
24. Auset M, Keller AA. Pore-scale processes that control dispersion of colloids in saturated porous media. *Water Resour Res*. 2004;40(3):W03503.
25. Bales RC, Gerba CP, Grondin GH, Jensen SL. Bacteriophage transport in sandy soil and fractured tuff. *Appl Environ Microbiol*. 1989;55(8):2061-2067.
26. Keller AA, Sirivithayapakorn S, Chrysikopoulos CV. Early breakthrough of colloids and bacteriophage MS2 in a water-saturated sand column. *Water Resour Res*. 2004;40(8):W08304.
27. Meyer DW, Bijeljic B. Pore-scale dispersion: bridging the gap between microscopic pore structure and the emerging macroscopic transport behavior. *Phys Rev E*. 2016;94(1):013107.
28. Brenner H, Gaydos LJ. The constrained brownian movement of spherical particles in cylindrical pores of comparable radius. *J Colloid Interface Sci*. 1977;58(2):312-356.
29. Deen WM. Hindered transport of large molecules in liquid-filled pores. *AICHE J*. 1987;33(9):1409-1425.
30. Stylianopoulos T, Diop-Frimpong B, Munn LL, Jain RK. Diffusion anisotropy in collagen gels and tumors: the effect of fiber network orientation. *Biophys J*. 2010;99(10):3119-3128.
31. Hansing J, Netz RR. Hydrodynamic effects on particle diffusion in polymeric hydrogels with steric and electrostatic particle–gel interactions. *Macromolecules*. 2018;51(19):7608-7620.
32. Lee YK, Porter C, Diamond SL, Crocker JC, Sinno T. Deposition of sticky spheres in channel flow: modeling of surface coverage evolution requires accurate sphere-sphere collision hydrodynamics. *J Colloid Interface Sci*. 2018;530:383-393.
33. Laal-Dehghani N, Christopher GF. 2D stokesian simulation of particle aggregation at quiescent air/oil-water interfaces. *J Colloid Interface Sci*. 2019;553:259-268.
34. Brenner H. Dispersion resulting from flow through spatially periodic porous media. *Philos Trans R Soc Lond, Ser A: Math Phys Sci*. 1980;297(1430):81-133.
35. Whitaker S. Flow in porous media I: a theoretical derivation of Darcy's law. *Transp Porous Media*. 1986;1(1):3-25.
36. Maier RS, Kroll DM, Bernard RS, Howington SE, Peters JF, Davis HT. Pore-scale simulation of dispersion. *Phys Fluids*. 2000;12(8):2065-2079.
37. Durlofsky L, Brady JF, Bossis G. Dynamic simulation of hydrodynamically interacting particles. *J Fluid Mech*. 1987;180:21-49.
38. Durlofsky L, Brady JF. Analysis of the Brinkman equation as a model for flow in porous media. *Phys Fluids*. 1987;30(11):3329-3341.
39. Phillips RJ, Brady JF, Bossis G. Hydrodynamic transport properties of hard-sphere dispersions. I. Suspensions of freely mobile particles. *Phys Fluids*. 1988;31(12):3462-3472.
40. Vitthal S, Sharma MM. A Stokesian dynamics model for particle deposition and bridging in granular media. *J Colloid Interface Sci*. 1992;153(2):314-336.
41. Phillips RJ, Deen WM, Brady JF. Hindered transport of spherical macromolecules in fibrous membranes and gels. *AICHE J*. 1989;35(11):1761-1769.
42. Phillips RJ, Deen WM, Brady JF. Hindered transport in fibrous membranes and gels: effect of solute size and fiber configuration. *J Colloid Interface Sci*. 1990;139(2):363-373.
43. He K, Khorasani FB, Retterer ST, Thomas DK, Conrad JC, Krishnamoorti R. Diffusive dynamics of nanoparticles in arrays of nanoposts. *ACS Nano*. 2013;7(6):5122-5130.
44. He K, Retterer ST, Srijanto BR, Conrad JC, Krishnamoorti R. Transport and dispersion of nanoparticles in periodic nanopost arrays. *ACS Nano*. 2014;8(5):4221-4227.
45. Jacob JDC, He K, Retterer ST, Krishnamoorti R, Conrad JC. Diffusive dynamics of nanoparticles in ultra-confined media. *Soft Matter*. 2015;11(38):7515-7524.
46. McGrath J, Jimenez M, Bridle H. Deterministic lateral displacement for particle separation: a review. *Lab Chip*. 2014;14(21):4139-4158.
47. de Beeck JO, Malsche WD, Moor PD, Desmet G. Hydrodynamic chromatography separations in micro- and nanopillar arrays produced using deep-UV lithography. *J Sep Sci*. 2012;35(15):1877-1883.

48. Daneyko A, Hlushkou D, Khirevich S, Tallarek U. From random sphere packings to regular pillar arrays: analysis of transverse dispersion. *J Chromatogr A*. 2012;1257:98-115.
49. Striegel AM, Brewer AK. Hydrodynamic chromatography. *Annu Rev Anal Chem*. 2012;5:15-34.
50. Stylianopoulos T, Poh MZ, Insin N, et al. Diffusion of particles in the extracellular matrix: the effect of repulsive electrostatic interactions. *Biophys J*. 2010;99(5):1342-1349.
51. Beenakker CWJ. Ewald sum of the Rotne-Prager tensor. *J Chem Phys*. 1986;85(3):1581-1582.
52. Bleibel J. Ewald sum for hydrodynamic interactions with periodicity in two dimensions. *J Phys A Math Theor*. 2012;45(22):225002.
53. Jeffrey DJ, Onishi Y. Calculation of the resistance and mobility functions for two unequal rigid spheres in low-Reynolds-number flow. *J Fluid Mech*. 1984;139:261-290.
54. Higham NJ. Cholesky factorization. *Wiley Interdiscip Rev: Comput Stat*. 2009;1(2):251-254.
55. Ermak DL, McCammon JA. Brownian dynamics with hydrodynamic interactions. *J Chem Phys*. 1978;69(4):1352-1360.
56. Banchio AJ, Brady JF. Accelerated Stokesian dynamics: Brownian motion. *J Chem Phys*. 2003;118(22):10323-10332.
57. Brady JF, Bossis G. Stokesian dynamics. *Annu Rev Fluid Mech*. 1988;20(1):111-157.
58. Phillips RJ, Brady JF, Bossis G. Hydrodynamic transport properties of hard-sphere dispersions. II. Porous media. *Phys Fluids*. 1988;31(12):3473-3479.
59. Wang M, Brady JF. Short-time transport properties of bidisperse suspensions and porous media: a Stokesian dynamics study. *J Chem Phys*. 2015;142(9):094901.
60. Adamczyk Z, Adamczyk M, van de Ven TGM. Resistance coefficient of a solid sphere approaching plane and curved boundaries. *J Colloid Interface Sci*. 1983;96(1):204-213.
61. van der Sman RGM. Effects of confinement on hydrodynamic interactions between a suspended sphere and stationary obstacles. *Comput Fluids*. 2012;58:63-69.
62. Chen SB. Driven transport of particles in 3D ordered porous media. *J Chem Phys*. 2013;139(7):074904.
63. Ghosh PK, Hänggi P, Marchesoni F, et al. Driven Brownian transport through arrays of symmetric obstacles. *Phys Rev E*. 2012;85(1):011101.
64. Souto HPA, Moyne C. Dispersion in two-dimensional periodic porous media. Part II. Dispersion tensor. *Phys Fluids*. 1997;9(8):2253-2263.
65. Edwards DA, Shapiro M, Brenner H, Shapira M. Dispersion of inert solutes in spatially periodic, two-dimensional model porous media. *Transp Porous Media*. 1991;6(4):337-358.
66. Koch DL, Cox RG, Brenner H, Brady JF. The effect of order on dispersion in porous media. *J Fluid Mech*. 1989;200:173-188.
67. Maier RS. Enhanced dispersion in cylindrical packed beds. *Philos Trans R Soc London, Ser A*. 2002;360(1792):497-506.
68. Howard MP, Gautam A, Panagiotopoulos AZ, Nikoubashman A. Axial dispersion of Brownian colloids in microfluidic channels. *Phys Rev Fluids*. 2016;1(4):044203.
69. Brenner H. Macrotransport processes. *Langmuir*. 1990;6(12):1715-1724.
70. Patel PD, Shaqfeh ESG. A computational study of DNA separations in sparse disordered and periodic arrays of posts. *J Chem Phys*. 2003;118(6):2941-2951.
71. Ou J, Cho J, Olson DW, Dorfman KD. DNA electrophoresis in a sparse ordered post array. *Phys Rev E*. 2009;79(6):061904.
72. Chakrabarti B, Gaillard C, Saintillan D. Trapping, gliding, vaulting: transport of semiflexible polymers in periodic post arrays. *Soft Matter*. 2020;16(23):5534-5544.
73. André P, Long D, Ajdari A. Polyelectrolyte/post collisions during electrophoresis: influence of hydrodynamic interactions. *Eur Phys J B*. 1998;4(3):307-312.
74. Hernández-Ortiz JP, Chopra M, Geier S, de Pablo JJ. Hydrodynamic effects on the translocation rate of a polymer through a pore. *J Chem Phys*. 2009;131(4):044904.
75. Rotne J, Prager S. Variational treatment of hydrodynamic interaction in polymers. *J Chem Phys*. 1969;50(11):4831-4837.
76. Jain A, Sunthar P, Dünweg B, Prakash JR. Optimization of a Brownian-dynamics algorithm for semidilute polymer solutions. *Phys Rev E*. 2012;85(6):066703.
77. Ramaswamy M, Lin NYC, Leahy BD, et al. How confinement-induced structures Alter the contribution of hydrodynamic and short-ranged repulsion forces to the viscosity of colloidal suspensions. *Phys Rev X*. 2017;7(4):041005.

How to cite this article: Mangal D, Conrad JC, Palmer JC. Nanoparticle dispersion in porous media: Effects of hydrodynamic interactions and dimensionality. *AIChE J*. 2021; 67:e17147. https://doi.org/10.1002/aic.17147

APPENDIX

Far-field resistance matrix

Far-field contributions to the HI were evaluated using the RP tensor.[75] The RP tensor for two spheres i and j located at positions $\mathbf{r}_i$ and $\mathbf{r}_j$, respectively, is defined as:[75]

$$\mathbf{M}_{ij}^{\mathrm{RP}} = \begin{cases} (6\pi\eta a_i)^{-1}\left\{\frac{3}{4}a_i r^{-1}(\mathbf{I}+\hat{\mathbf{r}}\hat{\mathbf{r}}) + \frac{1}{2}a_i\left(\frac{a_i^2+a_j^2}{2}\right)r^{-3}(\mathbf{I}-3\hat{\mathbf{r}}\hat{\mathbf{r}})\right\}, & i\neq j \\ (6\pi\eta a_i)^{-1}\mathbf{I}, & i=j \end{cases} \tag{A1}$$

where a_i and a_j are the spheres' radii, r is the norm of the separation vector $\mathbf{r}_{ij} = \mathbf{r}_j - \mathbf{r}_i$, $\hat{\mathbf{r}} = \mathbf{r}_{ij}/r$ is the unit vector, and $\mathbf{I}$ is the 3×3 identity matrix. Because of the long-ranged nature of the RP tensor, which decays slowly as $1/r$, it is typically computed using efficient Ewald summation techniques, rather than by direct evaluation using Equation (A1).

Ewald summation in 3D

The Ewald summation of the RP tensor for a 3D periodic system is given by:[51]

$$\mathbf{M}_{ij}^{\infty} = (6\pi\eta a_i)^{-1}\left\{\mathbf{I}\left(1-6\pi^{-1/2}a_i\alpha+\frac{40}{3}\pi^{-1/2}a_i^3\alpha^3\right)\delta_{ij} + \sum_{\mathbf{r}\neq 0}^{r<r_c}\mathbf{M}^{(1)}(\mathbf{r}) + V^{-1}\sum_{\mathbf{k}_r\neq 0}^{k_r<k_c}\mathbf{M}^{(2)}(\mathbf{k}_r)\cos(\mathbf{k}_r\cdot\mathbf{r}_{ij})\right\}, \tag{A2}$$

with

$$\mathbf{M}^{(1)}(\mathbf{r}) = \mathbf{I}\left\{\left(\frac{3}{4}a_i r^{-1} + \frac{1}{2}a_i\left(\frac{a_i^2+a_j^2}{2}\right)r^{-3}\right)\mathrm{erfc}(\alpha r) + \left(4\alpha^7 a_i\left(\frac{a_i^2+a_j^2}{2}\right)r^4 + 3\alpha^3 a_i r^2 - 20\alpha^5 a_i\left(\frac{a_i^2+a_j^2}{2}\right)r^2 - \frac{9}{2}\alpha a_i + 14\alpha^3 a_i\left(\frac{a_i^2+a_j^2}{2}\right) + \alpha a_i\left(\frac{a_i^2+a_j^2}{2}\right)r^{-2}\right)\pi^{-1/2}\exp\left(-\alpha^2 r^2\right)\right\} + \hat{\mathbf{r}}\hat{\mathbf{r}}\left\{\left(\frac{3}{4}a_i r^{-1} - \frac{3}{2}a_i\left(\frac{a_i^2+a_j^2}{2}\right)r^{-3}\right)\mathrm{erfc}(\alpha r) + \left(-4\alpha^7 a_i\left(\frac{a_i^2+a_j^2}{2}\right)r^4 - 3\alpha^3 a_i r^2 + 16\alpha^5 a_i\left(\frac{a_i^2+a_j^2}{2}\right)r^2 + \frac{3}{2}\alpha a_i - 2a_i\left(\frac{a_i^2+a_j^2}{2}\right)\alpha^3 - 3\alpha a_i\left(\frac{a_i^2+a_j^2}{2}\right)r^{-2}\right)\pi^{-1/2}\exp\left(-\alpha^2 r^2\right)\right\} \tag{A3}$$

$$\mathbf{M}^{(2)}(\mathbf{k}_r) = \left(\mathbf{I} - \hat{\mathbf{k}}\hat{\mathbf{k}}\right)\left(a_i - \frac{1}{3}a_i\left(\frac{a_i^2+a_j^2}{2}\right)k^2\right)\left(1 + \frac{1}{4}\alpha^{-2}k^2 + \frac{1}{8}\alpha^{-4}k^4\right) 6\pi k^{-2}\exp\left(-\frac{1}{4}\alpha^{-2}k^2\right), \tag{A4}$$

where V is the volume of the simulation cell, δ_{ij} is the Kronecker delta, $\mathbf{r} = \mathbf{r}_j - \mathbf{r}_i + \mathbf{n}$ is the separation vector, $\mathbf{n} = \{n_1L_x, n_2L_y, n_3L_z : n_i \in \mathbb{Z}\}$ is the lattice vector, $r = |\mathbf{r}|$, $\hat{\mathbf{r}} = \mathbf{r}/r$, $\mathbf{k}_r = \{2\pi n_1/L_x, 2\pi n_2/L_y, 2\pi n_3/L_z : n_i \in \mathbb{Z}\}$ is the reciprocal lattice vector, $k = |\mathbf{k}_r|$, $\hat{\mathbf{k}} = \mathbf{k}_r/k$, and L_x, L_y, and L_z are the x, y, and z dimensions of the simulation cell, respectively. The Ewald splitting parameter α determines the rate of convergence of the real and reciprocal space sums in Equation (A2). For our simulations we set $\alpha = 2/L$ where $L = (L_xL_yL_z)^{1/3}$, and correspondingly chose $r_c = 3.5/\alpha$ and $k_c = 7.0\alpha$ for the real and reciprocal space cutoffs, respectively. These parameter choices ensure near optimal computational efficiency and relative errors of less than 1×10^{-5} in evaluating the real and reciprocal space sums.[31,51,76]

Ewald summation in 2D

For systems with 2D periodicity in the x-y plane, analogous expressions for the Ewald summation of the RP tensor are given by:[52]

$$\mathbf{M}_{ij}^{\infty} = (6\pi\eta a_i)^{-1}\left\{\mathbf{I}\left(1 - \frac{3}{2}\pi^{-1/2}a_i\alpha - \frac{2}{3}\pi^{-1/2}a_i^3\alpha^3\right)\delta_{ij} + \sum_{\mathbf{r}\neq 0}^{r<r_c}\mathbf{M}^{(1)}(\mathbf{r}) + \sum_{\mathbf{k}_r\neq 0}^{k_r<k_c}\mathbf{M}^{(2)}(\mathbf{k}_r)\cos\left(\mathbf{k}_r\cdot\mathbf{r}_{ij}\right)\right\}, \tag{A5}$$

with

$$\mathbf{M}^{(1)}(\mathbf{r}) = \mathbf{I}\left\{\left(\frac{3}{4}a_i r^{-1} + \frac{1}{2}a_i\left(\frac{a_i^2+a_j^2}{2}\right)r^{-3}\right)\mathrm{erfc}(\alpha r) + a_i\left(\frac{a_i^2+a_j^2}{2}\right)\alpha r^{-2}\pi^{-1/2}\exp\left(-\alpha^2 r^2\right)\right\} + \hat{\mathbf{r}}\hat{\mathbf{r}}\left\{\left(\frac{3}{4}a_i r^{-1} - \frac{3}{2}a_i\left(\frac{a_i^2+a_j^2}{2}\right)r^{-3}\right)\mathrm{erfc}(\alpha r) + \left(-3a_i\left(\frac{a_i^2+a_j^2}{2}\right)\alpha r^{-2} + \frac{3}{2}a_i\alpha - 2a_i\left(\frac{a_i^2+a_j^2}{2}\right)\alpha^3\right)\pi^{-1/2}\exp\left(-\alpha^2 r^2\right)\right\} \tag{A6}$$

$$\mathbf{M}^{(2)}(\mathbf{k}_r) = \mathbf{I}\left\{2a_i\mathrm{erfc}\left(\frac{1}{2}k\alpha^{-1}\right)\right\}\frac{3}{2}\pi L^{-2}k^{-1} - \hat{\mathbf{k}}\hat{\mathbf{k}}\left\{\left(a - \frac{2}{3}a_i\left(\frac{a_i^2+a_j^2}{2}\right)k^2\right)\mathrm{erfc}\left(\frac{1}{2}k\alpha^{-1}\right) + a_i\alpha^{-1}k\pi^{-1/2}\exp\left(-\frac{1}{4}\alpha^{-2}k^2\right)\right\}\frac{3}{2}\pi L^{-2}k^{-1}, \tag{A7}$$

where $\mathbf{I}$ is the 2×2 identity matrix, $\mathbf{r} = \mathbf{r}_j - \mathbf{r}_i + \mathbf{n}$ is the separation vector, $\mathbf{n} = \{n_1L_x, n_2L_y : n_i \in \mathbb{Z}\}$ is the lattice vector, $\mathbf{k}_r = \{2\pi n_1/L_x, 2\pi n_2/L_y : n_i \in \mathbb{Z}\}$ is the reciprocal lattice vector, $L = (L_xL_y)^{1/2}$, and L_x and L_y are the x and y dimensions of the simulation cell, respectively. Following our calculations in 3D, Ewald parameters of $\alpha = 2/L$, $r_c = 3.5/\alpha$, and $k_c = 7.0\alpha$ were used in our 2D simulation.

Near-field lubrication correction

In low-Reyonlds-number flow, the hydrodynamic interactions between two particles i and j can be expressed as:[31,53]

$$\begin{bmatrix}\mathbf{F}_i\\ \mathbf{F}_j\end{bmatrix} = \begin{bmatrix}\mathbf{R}_{ii}^{2P} & \mathbf{R}_{ij}^{2P}\\ \mathbf{R}_{ji}^{2P} & \mathbf{R}_{jj}^{2P}\end{bmatrix}\cdot\begin{bmatrix}\mathbf{V}_i - \mathbf{V}_\infty(\mathbf{r}_i)\\ \mathbf{V}_j - \mathbf{V}_\infty(\mathbf{r}_j)\end{bmatrix}, \tag{B1}$$

where $\mathbf{V}_i$ and $\mathbf{V}_j$ are the particle velocities, $\mathbf{V}_\infty$ is the unperturbed fluid velocity at the particles' centers, and $\mathbf{R}^{2P}$ is the pair resistance matrix. The elements of $\mathbf{R}^{2P}$ are given by:

$$\mathbf{R}_{ij}^{2P} = \left(X_{ij} - Y_{ij}\right)\hat{\mathbf{r}}\hat{\mathbf{r}} + Y_{ij}\mathbf{I}, \tag{B2}$$

where X_{ij} and Y_{ij} are scalar functions that both depend on the rescaled variables $\lambda = a_j/a_i$ and $s = 2r/(a_i + a_j)$ and the scalar separation distance between the two spheres r.[53] The pair resistance matrix in Equation (B2) is singular at contact (i.e., at $r = a_i + a_j$). To avoid numerical issues associated with integrating the equations of motions near contact, we regularize the interactions at $r_{\min} = 1.0001(a_i + a_j)$, and

evaluate Equation (B2) at $r = r_{min}$ for all separation distances r less than this threshold.[77] The elements of the lubrication correction term $\mathbf{R}^{lub}$ in Equation (3) are obtained by subtracting the far-field contribution from the pair resistance matrix:

$$\mathbf{R}_{ii}^{lub} = \sum_{j=1\neq i}^{N_{np}+1} \left(\mathbf{R}_{ii}^{2P}(s,\lambda) - \left(\left(\mathbf{M}^{RP} \right)^{-1} \right)_{ii} (\mathbf{r}_{ij}) \right) \tag{B3}$$

$$\mathbf{R}_{ij}^{lub} = \mathbf{R}_{ij}^{2P}(s,\lambda) - \left(\left(\mathbf{M}^{RP} \right)^{-1} \right)_{ij} (\mathbf{r}_{ij}), \tag{B4}$$

where $(\mathbf{M}^{RP})^{-1}$ is the inverse of the two-particle RP mobility matrix. The computational cost associated with inverting $\mathbf{M}^{RP}$ at every iteration step can be mitigated by pre-tabulating submatrices $((\mathbf{M}^{RP})^{-1})_{ii}$ and $((\mathbf{M}^{RP})^{-1})_{ij}$ and using fit functions to evaluate these quantities during the simulations. Following Reference 31, we use fit functions of the form:

$$\left(\left(\mathbf{M}^{RP} \right)^{-1} \right)_{ii} = \sum_{n=0}^{n=6} \left(\frac{c_n}{s^n} \mathbf{I} + \frac{d_n}{s^n} \hat{\mathbf{r}}\hat{\mathbf{r}} \right) \tag{B5}$$

$$\left(\left(\mathbf{M}^{RP} \right)^{-1} \right)_{ij} = \sum_{n=0}^{n=6} \left(\frac{c'_n}{s^n} \mathbf{I} + \frac{d'_n}{s^n} \hat{\mathbf{r}}\hat{\mathbf{r}} \right), \tag{B6}$$

where c_n, c'_n, d_n, and d'_n are fit parameters.

Modified-midpoint scheme

The modified-midpoint scheme is a fast numerical method for calculating the divergence of the resistance matrix,[56] which appears in the particle evolution equation (Equation (4)). In this scheme, the velocity without drift for the particle at the current position $\mathbf{r}^0$ is calculated via:

$$\mathbf{V}(\mathbf{r}^0) = \left(\mathbf{R}_{ii}^{FU} \right)^{-1} (\mathbf{r}^0) \cdot \left[\mathbf{F}_i^B(\mathbf{r}^0) + \mathbf{F}_i^C(\mathbf{r}^0) \right]. \tag{C1}$$

Next, the particle is moved along the direction of $\mathbf{V}(\mathbf{r}^0)$ to an intermediate position $\mathbf{r}'$ using

$$\mathbf{r}' = \mathbf{r}^0 + \mathbf{V}(\mathbf{r}^0) \Delta t', \tag{C2}$$

where $\Delta t' = dt/m$ and m is a positive integer. The value of m is chosen to be large ($m = 200$ in our simulations) to ensure a small fractional time step and hence a small displacement $\mathbf{r}' - \mathbf{r}^0$ such that the divergence of the resistance matrix can be approximated using the finite-difference formula:

$$\nabla \cdot \left(\mathbf{R}_{ii}^{FU} \right)^{-1} (t) = \frac{dt}{2\Delta t'} \left[\left(\mathbf{R}_{ii}^{FU} \right)^{-1} (\mathbf{r}') - \left(\mathbf{R}_{ii}^{FU} \right)^{-1} (\mathbf{r}^0) \right] \cdot \left[\mathbf{F}_i^B(\mathbf{r}^0) + \mathbf{F}_i^C(\mathbf{r}^0) \right]. \tag{C3}$$